

# DeEPeR: Enhancing Performance and Reliability in Chip-Scale Optical Interconnection Networks

Mahdi Nikdast<sup>1</sup>, Gabriela Nicolescu<sup>2</sup>, Jelena Trajkovic<sup>3</sup>, and Odile Liboiron-Ladouceur<sup>4</sup>

<sup>1</sup>Colorado State University, CO, USA <sup>2</sup>Polytechnique Montréal, QC, Canada

<sup>3</sup>Concordia University, QC, Canada <sup>4</sup>McGill University, QC, Canada

Mahdi.Nikdast@colostate.edu

## ABSTRACT

This paper presents an efficient device-level design method to enhance the performance and reliability (DeEPeR) in optical interconnection networks (OINs) under fabrication process variations (PV). Considering different range of variations, DeEPeR explores the design space of fundamental optical components in OINs (e.g., microresonators (MRs)) to improve the overall system performance and reliability. Our study also includes the design and fabrication of several MRs to experimentally validate our proposed method. Moreover, as a system-level case study, we apply DeEPeR to a general passive OIN under PV. Results indicate that DeEPeR considerably improves the optical signal-to-noise ratio (OSNR) in optical interconnection networks.

## CCS CONCEPTS

• **Hardware** → **Photonic and optical interconnect; Process variations; Hardware reliability;**

## KEYWORDS

Silicon Photonic Interconnects; MPSoCs; Process Variations; Reliability

### ACM Reference Format:

Mahdi Nikdast<sup>1</sup>, Gabriela Nicolescu<sup>2</sup>, Jelena Trajkovic<sup>3</sup>, and Odile Liboiron-Ladouceur<sup>4</sup>. 2018. DeEPeR: Enhancing Performance and Reliability in Chip-Scale Optical Interconnection Networks. In *GLSVLSI '18: 2018 Great Lakes Symposium on VLSI, May 23–25, 2018, Chicago, IL, USA*. ACM, New York, NY, USA, 6 pages. <https://doi.org/10.1145/3194554.3194566>

## 1 INTRODUCTION

Multiprocessor systems-on-chip (MPSoCs) are continuously scaling to support new applications demands, such as higher computation and communication bandwidth required for emerging big data applications. The inter- and intra-chip communication in MPSoCs need to keep pace with such rapidly growing requirements. Compared with conventional metallic interconnects, optical interconnection networks (OINs) can outperform MPSoCs through realizing an ultra-high bandwidth and low-latency communication with a low power consumption [1]. The bandwidth performance in OINs

can be further improved through employing wavelength-division multiplexing (WDM), which allows simultaneous transmission of multiple optical wavelengths in a single waveguide.

Several WDM-based OINs have been proposed for MPSoCs [15], in which hundreds and thousands of microresonators (MRs) are integrated. These fundamental components, however, are considerably sensitive to fabrication process variations (PV) [6]. Particularly, while different MRs need to be precisely matched in terms of their central wavelengths (e.g., the resonant wavelength in MRs) to achieve a reliable communication in OINs, PV deviate MRs resonant wavelengths, resulting in performance and reliability degradation in OINs. Silicon-on-insulator (SOI) thickness and waveguide width variations, considered in this work, are the major concerns in silicon photonics fabrication [3, 6]. PV stem from optical lithography imperfection and are inevitable in OINs, necessitating developing efficient design methods to compensate for such variations.

Fabrication process variations have been studied in OINs at both device-level [3, 6] and system-level [9, 13, 14]. Several methods have been proposed to compensate for PV, and specifically to restore the resonant wavelength of MRs. The first type of solutions is to use high-energy particles, such as UV light, to adjust the refractive index of waveguides, and hence the resonant wavelength of MRs [8]. However, this technique is not applicable to systems consisting of a large number of MRs due to its complexity, and it degrades the quality factor (i.e.,  $Q$ ) of MRs. The second type of solutions (a.k.a. trimming) is to use thermal tuning to increase the wavelength (i.e., red shift), and current injection to decrease the wavelength (i.e., blue shift). Thermal tuning, however, is power hungry, while current injection has a limited correction range and imposes an extra power loss. Nevertheless, trimming is required to compensate for thermal variations and when using active devices and OINs.

Some efforts have been also made to develop different system-level design methods to compensate for PV in OINs. A reliability design flow to outperform OINs under process and thermal variations was proposed in [12], which is based on using thermal tuning and MR channel remapping. In [5], a framework was proposed to alleviate the impact of crosstalk noise in physically trimmed OINs under PV, improving the performance in such networks, but at a cost of a high power overhead (i.e., 50% on average).

The novel contribution of this paper is in developing an efficient device-level design method to enhance the performance and reliability (DeEPeR) in OINs under fabrication process variations. Considering different range of variations, DeEPeR explores the design space of MRs to study how employing different design parameters in such components impacts the performance and reliability at the device- and system-level. We consider strip waveguides, which are used for routing in OINs and passive devices (e.g., MRs, filters)

Permission to make digital or hard copies of all or part of this work for personal or classroom use is granted without fee provided that copies are not made or distributed for profit or commercial advantage and that copies bear this notice and the full citation on the first page. Copyrights for components of this work owned by others than ACM must be honored. Abstracting with credit is permitted. To copy otherwise, or republish, to post on servers or to redistribute to lists, requires prior specific permission and/or a fee. Request permissions from [permissions@acm.org](mailto:permissions@acm.org).

*GLSVLSI '18, May 23–25, 2018, Chicago, IL, USA*

© 2018 Association for Computing Machinery.

ACM ISBN 978-1-4503-5724-1/18/05...\$15.00

<https://doi.org/10.1145/3194554.3194566>

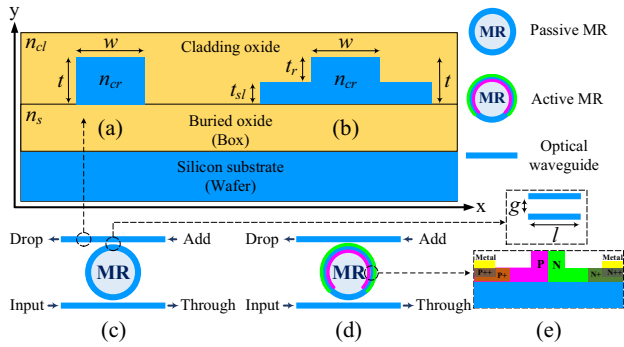


**Figure 1: (a) and (b): Cross sections of a strip and a ridge waveguide; (c) and (d): an overview of a passive and an active MR; and (e): a P-N junction.**

and networks, as well as ridge waveguides, which are employed in active devices (e.g., MR modulators) and OINs.

At the device-level, considering waveguides with various design parameters, DeEPeR comprehensively studies the impact of different variations on the resonant wavelength of passive and active MRs. Also, our study includes the design and fabrication of several MRs using DeEPeR to experimentally validate the proposed method, as well as demonstrating the efficiency of DeEPeR when it is employed in a device fabrication. Indicating the impact of DeEPeR at the system-level, we apply our method to a case study of a general passive WDM-based OIN, which can be applied to any specific passive OIN, under random PV. Results indicate that DeEPeR considerably improves the optical signal-to-noise ratio (OSNR) in the system (almost 6 dB improvement in the OSNR on average). The OSNR denotes the received optical signal quality and it impacts the bit error rate (BER) in a system, hence determining the performance and reliability. This paper does not consider thermal variations.

The rest of the paper is organized as follows. In Section 2, we present the fundamental concepts and the theory of strip and ridge waveguides as well as MR-based devices. Section 3 presents our proposed method, DeEPeR, and includes our fabrication details and results. The case study of the general passive OIN architecture and its results are presented in Section 4. Finally, we draw conclusions in Section 5.

## 2 OPTICAL WAVEGUIDES AND MRs

This section reviews some fundamental concepts in waveguides and MRs. In general, optical devices can be classified as passive or active (see Fig. 1). Strip waveguides are used in passive devices and OINs (i.e., optical signal transmits passively), while ridge waveguides are widely employed in electro-optic devices (i.e., active devices) as they allow for electrical connections to be made to the waveguides (see Figs. 1(d) and 1(e)). This paper considers the variations in the SOI thickness and waveguide width, and doping variations related to active devices are not considered.

### 2.1 Strip and Ridge Waveguides

Figs. 1(a) and 1(b) indicate cross sections of a strip and a ridge waveguide, respectively. As can be seen, the waveguide core, with a refractive index of  $n_{cr}$ , is buried in a cladding oxide layer at the top, with a refractive index of  $n_{cl}$ , and a substrate oxide layer at

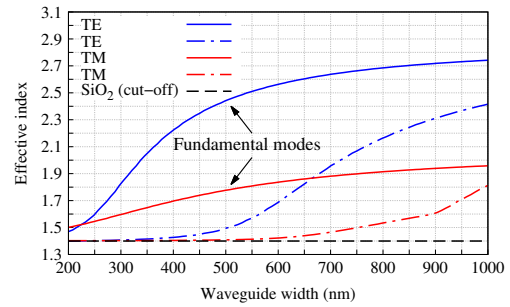


**Figure 2: Effective indices of different waveguide modes in a strip waveguide for a SOI thickness of 220 nm ( $t = 220$  nm) and  $\lambda = 1550$  nm).**

the bottom, whose refractive index is  $n_s$ . Note that  $n_{cr} > n_{cl,s}$ , and hence the optical signal is confined in the waveguide core. In this work, we consider symmetric waveguides in which  $n_{cl} = n_s$ . Also, the waveguide core is from silicon (Si) while the cladding and substrate are from silicon dioxide (SiO<sub>2</sub>). According to Fig. 1(a), the strip waveguide has a width of  $w$  and a thickness of  $t$ . Similarly, the ridge waveguide, indicated in Fig. 1(b), has a slab with a thickness of  $t_{sl}$ , as well as a ridge with a width of  $w$  and a thickness of  $t_r$  on the top (i.e.,  $t = t_{sl} + t_r$  and  $t_r > t_{sl}$ ). Note that the etching depth and the SOI thickness determine  $t_r$  (and hence  $t_{sl}$ ) and  $t$ , respectively.

One of the major parameters that determines different characteristics of optical waveguides is the effective index. The effective index quantifies the overall phase delay per unit length in a waveguide, relative to the phase delay in vacuum [7]. It highly depends on the optical wavelength and the dimensions of the waveguide. Given the original dimensions of an optical waveguide ( $w$  and  $t$  in Fig. 1), the effective index can be calculated as:

$$n_{eff}(\lambda, w, t) = \frac{\beta(\lambda, w, t)\lambda}{2\pi}, \quad (1)$$

in which  $\lambda$  is the optical wavelength. Also,  $\beta$  is the propagation constant of the optical mode, which we define shortly, in the waveguide that determines how the amplitude and phase of the light varies along the propagation direction. Numerical solutions of  $\beta$  in strip and ridge waveguides can be obtained using various numerical methods.

The effective index in waveguides also depends on the waveguide mode in which the light propagates. A waveguide mode is a transverse field pattern that propagates along the waveguide without changing amplitude and polarization profiles [7]. For instance, based on (1) and employing MODE [10], which is a commercial-grade simulator eigenmode solver and propagator, Fig. 2 indicates the effective indices of different waveguide modes in a strip waveguide when the optical wavelength ( $\lambda$ ) is 1550 nm,  $200 \text{ nm} \leq w \leq 1000 \text{ nm}$ , and  $t = 220 \text{ nm}$ . As can be seen, two types of optical modes exist in the waveguide, including transverse electric (TE) and transverse magnetic (TM) modes. When the effective index of a mode is larger than the refractive index of the cladding/substrate (i.e., SiO<sub>2</sub> in Fig. 2), then the mode is guided (i.e., it propagates in the waveguide along its longitudinal direction). Based on Fig. 2, strip waveguides with  $w < \approx 450 \text{ nm}$  and  $t = 220 \text{ nm}$  only supports a single mode (i.e., one TE and one TM mode, which are called the fundamental modes). Also, as the waveguide width increases (i.e.,  $w \gg 450 \text{ nm}$ ), more

optical modes are being excited in the waveguide (i.e., multi-mode waveguides). Similar trends can be observed for different optical modes in ridge waveguides.

## 2.2 MR-Based Add-Drop Filters and Switches

Strip waveguides can form passive MR-based add-drop filters, as shown in Fig. 1(c). Similarly, as depicted in Fig. 1(d), active MR-based switches can be constructed using ridge waveguides. Such devices can filter/switch an optical signal based on the resonant wavelength of the MR,  $\lambda_{MR}$ , and the wavelength of the input optical signal,  $\lambda$ : when  $\lambda = \lambda_{MR}$ , the optical signal is dropped from the input port towards the drop port (i.e., the MR is on resonance), while it propagates towards the through port when  $\lambda \neq \lambda_{MR}$  (i.e., the MR is off resonance). It is worth mentioning that the optical characteristics of active MRs (e.g., the resonant wavelength) can be dynamically altered by changing their effective indices through the thermo-optic or electro-optic effects. For example, Fig. 1(e) indicates a P-N junction based structure doped on a ridge waveguide that can be used to apply a reverse biased voltage to change the resonant wavelength of the MR. We detail some of the common properties of passive and active MRs in the following.

An MR is on resonance when the wavelength of the input optical signal ( $\lambda$ ) matches a whole number of times inside the optical length of the MR [4]:

$$\lambda_{MR}(\lambda, w, t) = \frac{n_{eff}(\lambda, w, t) \cdot (2\pi r + 2l)}{m}, \quad (2)$$

in which  $\lambda_{MR}$  is the resonant wavelength,  $m$  is an integer number that denotes the order of the resonant mode,  $r$  is the MR radius, and  $l$  is the coupler length (see Fig. 1(c)). Process variations change the width, and hence the radius, as well as the thickness of MRs, and consequently, shift the resonant wavelength in such devices. We assume that the variations on the input waveguide and the MR are the same. Considering the first order approximation of the waveguide dispersion [4], the resonant wavelength shift ( $\Delta\lambda_{MR}$ ) in an MR under PV can be calculated as:

$$\Delta\lambda_{MR}(\lambda, w', t') = \frac{\Delta v_{w,t} n_{eff} \cdot \lambda}{n_{eff}(\lambda, w, t) - \lambda \cdot \frac{\partial n_{eff}(\lambda, w, t)}{\partial \lambda}}. \quad (3)$$

Here,  $w' = w \pm v_w$  and  $t' = t \pm v_t$ , where  $v_w$  and  $v_t$  are the variations in the waveguide width and thickness, respectively. Also,  $\Delta v_{w,t} n_{eff}$  denotes the effective index changes due to the waveguide width and thickness variations.

## 3 DeEPeR: ENHANCING PERFORMANCE AND RELIABILITY IN OINs

This section studies the design space of MRs under PV, and presents different design guidelines required to apply DeEPeR to OINs. Also, we experimentally validate DeEPeR using fabrication results in this section.

### 3.1 DeEPeR: MRs Design Space

DeEPeR studies the impact of the different design parameters in waveguides (i.e.,  $w$  and  $t$ ) on the resonant wavelength shift in MRs. As SOI wafers have a standard thickness (e.g.,  $t = 220$  or  $300$  nm [16]),  $t$  cannot be freely altered during the design, and  $t_{r,sl}$  depends

on the available etching depths in the fabrication. Nevertheless, the waveguide width can be determined during the design process. Based on (3), the resonant wavelength shift in MRs depends on the waveguide width ( $w$ ). Therefore, DeEPeR explores how altering  $w$  impacts the resonant wavelength shift in MRs. Firstly, DeEPeR studies and distinguishes between the impacts of the waveguide width and the thickness variations on the resonant wavelength (i.e., resonant wavelength shift slopes in (4)). Secondly, considering these impacts altogether, DeEPeR evaluates the total resonant wavelength shift in MRs at different waveguide widths (see (5)).

Employing (3), we found out that the resonant wavelength in MRs changes almost linearly with the variations in the waveguide width and thickness. As a result, the resonant wavelength shift slope, when the waveguide width varies for example (i.e.,  $\frac{\partial \lambda_{MR}}{\partial w}$ ), can be approximated as:

$$\frac{\partial \lambda_{MR}}{\partial w} = \left| \frac{\Delta \lambda_{MR}(\lambda, w + v_w, t) - \Delta \lambda_{MR}(\lambda, w - v_w, t)}{2v_w} \right|. \quad (4)$$

Similarly, we can define  $\frac{\partial \lambda_{MR}}{\partial t}$ , which are the resonant wavelength shift slopes with respect to the variations in the ridge ( $v_{tr}$ ) and waveguide thickness ( $v_t$ ). Note that  $v_{tr}$  is related to the etching depth variations in the case of active MRs. Considering  $\frac{\partial \lambda_{MR}}{\partial w, t_r, t}$ , the total resonant wavelength shift ( $\Delta^T \lambda_{MR}$ ), due to the variations in the width as well as ridge and waveguide thickness altogether, is defined as:

$$\Delta^T \lambda_{MRp/a}(\lambda, w', t') = \sigma_t \left( \frac{\partial \lambda_{MR}}{\partial w} \alpha_{p/a} + \frac{\partial \lambda_{MR}}{\partial t_r} \alpha_a + \frac{\partial \lambda_{MR}}{\partial t} \right). \quad (5)$$

Here, the subscripts  $p$  and  $a$  denote the use of passive and active MRs, respectively. Moreover,  $\alpha_p = \frac{\sigma_w}{\sigma_t}$  is the ratio between the standard deviation associated with the waveguide width (i.e.,  $\sigma_w$ ) and thickness (i.e.,  $\sigma_t$ ) variations. Also, when using active MRs, we have  $\alpha_a = \frac{\bar{\sigma}_{w, tr}}{\sigma_t}$ , in which  $\bar{\sigma}_{w, tr}$  is the arithmetic mean between  $\sigma_w$  and  $\sigma_{tr}$ . Note that  $\sigma_{w, tr, t}$  can denote within-die, within-wafer, or wafer-to-wafer variations, and can be quantified through different fabrications or obtained from the fabrication vendor.

Employing (4) and MODE [10], we quantitatively simulate the resonant wavelength shift slopes for passive and active MRs in Figs. 3(a) and 3(b), respectively. Results are indicated for the fundamental TE mode (see Fig. 2). Also, we consider different waveguide widths ( $x$ -axis in the figures) while  $t = 220$  nm,  $t_{sl} = 90$  nm, and  $\lambda = 1550$  nm. As can be seen, the impacts of waveguide width and thickness variations on the resonant wavelength shift in MRs are different. For example, passive MRs with  $w > \approx 360$  nm (see Fig. 3(a)) are more tolerant against width variations compared with thickness variations. The fundamental mode confines better in the waveguide core as the waveguide width increases. As a result, the variations in the waveguide width have less impact on the TE mode distribution in wider waveguides, in which the impact of thickness variations is higher and dominant. Similar trends can be noticed in the case of active MRs, while such MRs are also sensitive to the variations in the ridge thickness (see  $\frac{\partial \lambda_{MR}}{\partial t_r}$  in Fig. 3(b)).

Using (5), Fig. 3(c) indicates the total resonant wavelength shift ( $\Delta^T \lambda_{MR}$ ) in passive and active MRs. Note that the  $z$ -axis denotes

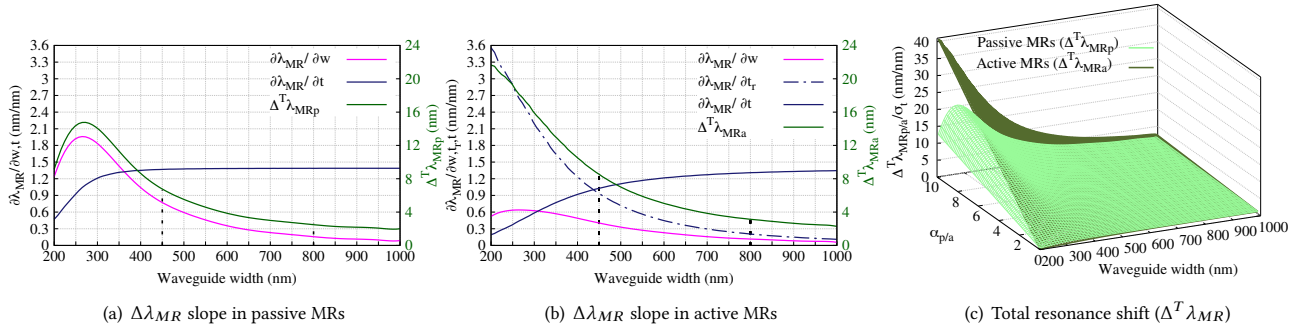


**Figure 3: (a) and (b): Resonant wavelength shift ( $\Delta\lambda_{MR}$ ) slopes; and (c): the total resonant wavelength shift ( $\Delta^T\lambda_{MR}$ ) in passive and active MRs for different waveguide widths ( $t = 220$  nm,  $t_{sl} = 90$  nm, and  $\lambda = 1550$  nm).**

$\frac{\Delta^T\lambda_{MR}}{\sigma_t}$ . As can be seen,  $\Delta^T\lambda_{MRp/a}$  highly depends on the MR waveguide width as well as  $\alpha_{p/a}$ . Given an  $\alpha_{p/a}$ , the total resonant wavelength shift decreases with an increase in the waveguide width due to the better confinement of the fundamental mode. For example, Figs. 3(a) and 3(b) depict the total resonant wavelength shift (green lines) in, respectively, passive ( $\Delta^T\lambda_{MRp}$ ) and active ( $\Delta^T\lambda_{MRa}$ ) MRs when  $\sigma_w = 7$  nm,  $\sigma_{t_r} = 5$  nm, and  $\sigma_t = 1$  nm [16], and hence  $\alpha_p = 7$  and  $\alpha_a = 6$ . As can be seen,  $\Delta^T\lambda_{MRp/a}$  drops as the waveguide width increases, and this reduction is significant when  $200$  nm  $\leq w < 450$  nm and it further improves for  $w > 450$  nm (the waveguide transits from single-mode to multi-mode when  $w \gg 450$  nm). Given a waveguide width in Fig. 3(c),  $\Delta^T\lambda_{MRp/a}$  rises with an increase in  $\alpha_{p/a}$ . When  $\alpha_{p/a}$  increases, more variations are introduced to the MRs, resulting in a higher total resonant wavelength shift. A wider waveguide can be employed to compensate for such higher variations.

### 3.2 DeEPeR: Design Guidelines

This section summarizes different steps required to apply DeEPeR to OINs. Based on Fig. 3, the impact of waveguide width variations is negligible when the waveguides are wide enough. Moreover, thickness variations, which become steady as  $w$  increases (see Figs. 3(a) and 3(b)), are the dominant contributor to the resonant wavelength shift. Also, the total resonant wavelength shift is higher for  $w \lesssim 450$  nm and its improvement is negligible when  $w \gtrsim 800$  nm (i.e., increasing the waveguide width barely affects the resonant wavelength shift). Therefore, depending on the expected range of variations ( $\alpha_{p/a}$  in Fig. 3(c)), designers can employ DeEPeR to optimize MRs design, minimizing  $\Delta^T\lambda_{MR}$  based on  $450$  nm  $\leq w \leq 800$  nm (when  $t = 220$  nm), and  $\kappa \geq \kappa'$ , where  $\kappa'$  is a minimum coupling required in the MR under design (step 1). Note that the cross-over coupling ( $\kappa$ ) can be improved considering different gaps and coupler lengths in the MR ( $g$  and  $l$  in Fig. 1).

Waveguides with  $w \gtrsim 450$  nm support multiple optical modes (see Fig. 2). While multi-mode waveguides could be used for mode-division multiplexing (MDM) in OINs, WDM-based OINs are very often designed for a single mode operation. Avoiding the excitation of higher order modes when using DeEPeR, we propose employing waveguide tapers (see Fig. 5) when applying DeEPeR to OINs (step 2). Using a waveguide taper to connect two waveguides with different widths of  $w_1$  and  $w_2$ , where  $w_2 > w_1$ , the taper length,

$L_t$ , should be long enough to avoid sudden changes in the waveguide width, and hence avoid exciting higher-order modes in the wider waveguide. We numerically simulated waveguides of different widths in MODE [10], and found out that considering  $L_t$  (in  $\mu\text{m}$ ) =  $\lfloor \frac{w_2 - w_1}{100 \text{ nm}} \rfloor \times 10 \mu\text{m}$  can safely avoid exciting higher-order modes when connecting waveguides of different widths. Moreover, waveguide tapers are required when entering and exiting waveguide bendings (higher-order modes can be excited in wide waveguides as they bend). Also, MR structures can be engineered to mitigate the impact of higher-order modes [11]. Finally, when using DeEPeR, designers need to leave enough space for routing as well as for electrical contacts (for active MRs).

### 3.3 DeEPeR: Fabrication and Validation

We designed two passive MR-based add-drop filters to experimentally validate DeEPeR and demonstrate its efficiency. Ten identical copies of the designed layout, shown in Fig. 4(a), were placed on a  $1.2 \times 0.8$  mm<sup>2</sup> chip fabricated by the Electron Beam (EBeam) Lithography facility at Applied NanoTools Incorporation. Each device is connected to three grating couplers designed for 1550 nm TE operation. Conventional  $500$  nm  $\times$   $220$  nm strip waveguides are used for routing. According to step 1, we assess the impact of DeEPeR on  $\Delta^T\lambda_{MR}$  at the proposed  $w$  range lower and upper bounds. As a result, in MR1 (without DeEPeR) indicated in Fig. 4(a), we consider  $220$  nm thick SOI strip waveguides with a  $400$  nm width connected to a TE polarization MR with a  $6.1 \mu\text{m}$  radius, and a coupler length and gap ( $l$  and  $g$  in Fig. 1(c)) of  $2 \mu\text{m}$  and  $200$  nm, respectively. Considering MR2 (with DeEPeR) in Fig. 4(a), the waveguide width increases to  $800$  nm, and the coupler length and the gap in the MR change to, respectively,  $6 \mu\text{m}$  and  $100$  nm, in order to improve the coupling between the input waveguide and the MR. Both MRs have a free-spectral range (FSR), which is the spacing between two consecutive resonances, of  $12$  nm, and are designed to resonate at  $1550$  nm. The MRs are placed as close as possible on the chip (i.e.,  $3 \mu\text{m}$ , the minimum distance allowed in the fabrication) to make sure they experience similar variations. Several waveguide tapers are considered in the layout to avoid exciting higher-order modes as well as terminating optical waveguides.

We carefully tested all the MRs (ten identical copies per each MR) and the measured through and drop port responses around  $1550$  nm are indicated in Fig. 4(b) for MR1 and MR2. The resonant peaks (ten per each MR) are specified as circles in Fig. 4(b). During

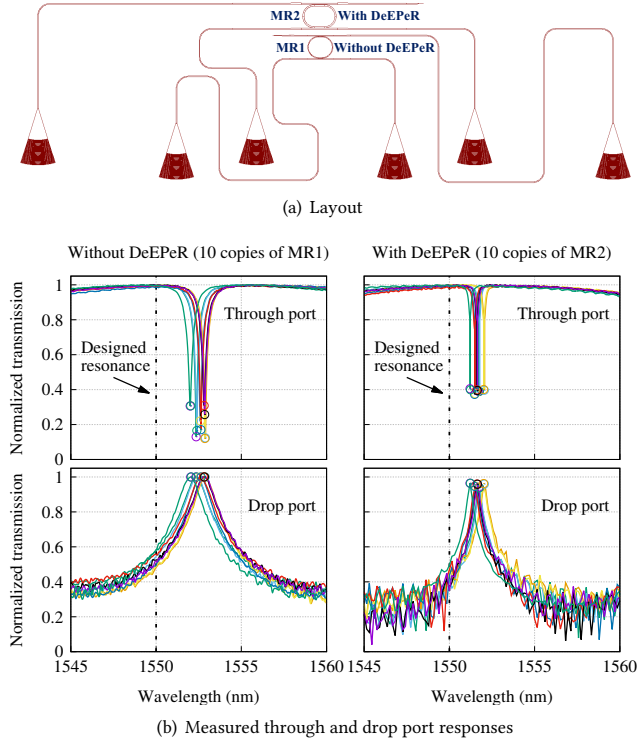


**Figure 4: (a) Layout of the fabricated MRs; and (b): measured through and drop port responses of the fabricated MRs without and with using DeEPeR.**

the test, the chip was located on a thermal heater to eliminate thermal variations. As can be seen, the resonant peaks are much closer to the designed resonance (i.e., 1550 nm) in case of using DeEPeR. On average, the total resonant wavelength shift without using DeEPeR (MR1) is 2.6 nm, and it reduces to 1.6 nm when DeEPeR is applied (MR2). In the best-case, the shift is only 1 nm when DeEPeR is employed, while it is as worse as 3 nm without using DeEPeR, indicating the advantage of using DeEPeR. Note that the measured drop port response in MR2 is slightly noisier due to a weaker coupling between the input waveguide and MR2, which can be further improved by using a longer (smaller) coupler (gap) in MR2. Nevertheless, a good Lorentzian response is captured. The data from the fabrication vendor indicates that the within-wafer  $\sigma_t$  and  $\sigma_w$  are 10 nm and 5 nm, respectively (i.e.,  $\alpha_p = 0.5 < 1$ ). Based on Fig. 3(c), when  $\alpha_p < 1$ ,  $\Delta^T \lambda_{MRp}$  slightly improves when  $w$  increases from 400 nm (in MR1) to 800 nm (in MR2). It is worth mentioning that the fabrication cost is related to the chip exposure area in  $\text{mm}^2$ , and hence employing DeEPeR to partially increase the waveguides widths (i.e., a few hundred nms) has a negligible impact on the fabrication cost.

#### 4 CASE STUDY AND RESULTS

This section explores the impact of DeEPeR on OINs at the system-level. We consider a case study of a general passive WDM-based OIN in MPSoCs, shown in Fig. 5, supporting  $n$  different wavelengths, and hence  $n$  processing cores. The case study represents an interconnect with several wavelength-selective optical switches ( $n \times m$  in

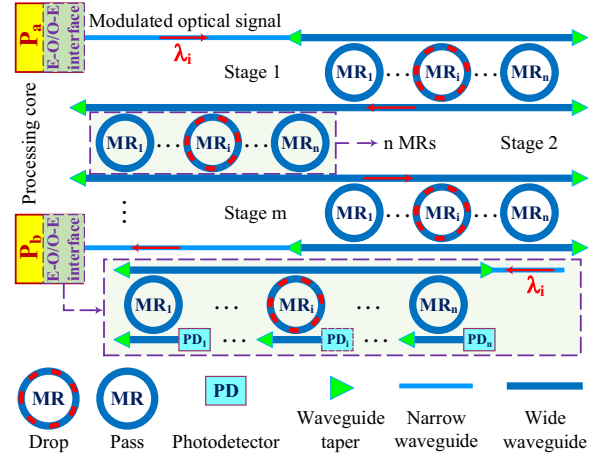


**Figure 5: An overview of the general passive WDM-based OIN supporting  $n$  optical wavelengths and employing DeEPeR.**

our model) and photodetectors (PDs,  $n$  PDs in our model) between two arbitrary processing cores in any passive WDM-based OIN. For simplicity, we explore the impact of PV on passive devices, and similar studies can be performed for the case of active devices. In Fig. 5, the source processing core  $P_a$  is communicating with the destination processing core  $P_b$  through the optical wavelength  $\lambda_i$ . The electrical-optical (E-O) interface is responsible for modulating the optical signal. When the optical signal on the wavelength  $\lambda_i$  matches the resonant wavelength of MR <sub>$i$</sub>  (i.e.,  $\lambda_i = \lambda_{MR_i}$  in Fig. 5), it couples to that MR and proceeds to the next switching stage ( $m$  switching stages in total), while it passes the MRs whose resonant wavelengths are different. Ultimately, it is detected at the PDs located at the end of the communication line in the optical-electrical (O-E) interface.

When optical signals are passing MRs, they suffer from some power loss and some crosstalk noise can be accumulated on the desired optical signal as well [2]. Also, PV shift the resonant wavelengths of the MRs, resulting in extra power loss and, most importantly, extra crosstalk noise. MRs with shifted resonant wavelengths drop fractions of the desired optical signal power, all of which can be accumulated at the PDs as crosstalk. In this paper, we consider the first-order in-band coherent crosstalk that cannot be filtered. Considering the desired optical signal power and the interfering crosstalk noise power received at the PDs (before detection), the OSNR associated with the optical wavelength  $\lambda_i$  can be defined as (in dB):

$$OSNR(\lambda_i, w', t') = 10 \log_{10} \frac{S_p(\lambda_i, w', t')}{N_p(\lambda_i, w', t')}, \quad (6)$$

where  $S_p$  and  $N_p$  are, respectively, the desired optical signal power and the crosstalk noise power received at the PD <sub>$i$</sub> . We study the impact of DeEPeR on the OSNR as it determines the received optical signal quality and also the BER in a system, and hence the performance and reliability.

We consider  $n = m = 4$  (see Fig. 5) with passive MRs of radii 5  $\mu\text{m}$  and couplers with a length of 2  $\mu\text{m}$ , and hence an FSR of 15 nm. Each MR's radius is slightly different to cover the whole wavelength range. Furthermore,  $\lambda = 1550$  nm and  $g = 200$  nm (see Fig. 1(c)).

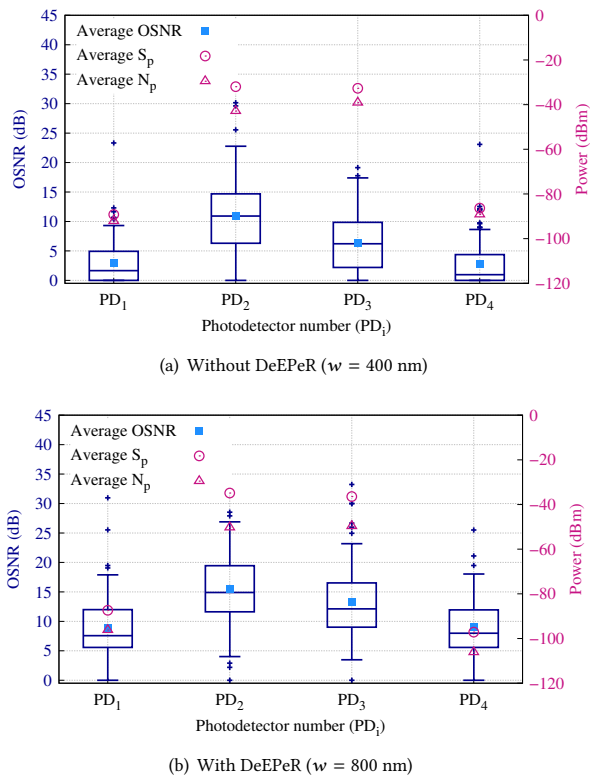


**Figure 6: The OSNR as well as the average desired signal and crosstalk noise power calculated at different PDs in the general passive WDM-based OIN in Fig. 5 without and with using DeEPer ( $t = 220$  nm).**

A channel spacing of 4 nm is assumed:  $\lambda_1 = \lambda_{MR1} = 1550$  nm and  $\lambda_4 = \lambda_{MR4} = 1562$  nm. The laser output optical power in the E-O interface is 0 dBm, and the chip size is  $1 \text{ cm}^2$  (for propagation loss analysis). Also, an average propagation loss of 2 dB/cm is considered when using narrow and wide waveguides. Considering  $\sigma_w = 7$  nm and  $\sigma_t = 1$  nm [16] (see Section 3.1), and based on a normal distribution, we randomly generate 100 PV maps, each of which has 20 points ( $n = 4 \times m = 4$  and four MRs connected to the PDs), and apply them to the OIN in Fig. 5. DeEPer is implemented in our in-house simulator, which is also used to calculate the resonant wavelength shift in the MRs and also  $S_p$  and  $N_p$  (see(6)) received at each PD (before detection).

Fig. 6 depicts the OSNR (box-plots) at each photodetector (x-axis) in the OIN without and with employing DeEPer when  $t = 220$  nm. Similar to the fabrication, we consider  $w = 400$  nm and  $w = 800$  nm in Figs. 6(a) and 6(b), respectively. As can be seen, the OSNR at each PD increases when using DeEPer: the average OSNR over all the PDs equals 5.8 dB without using DeEPer, and it increases to 11.7 dB when DeEPer is applied (i.e., almost 6 dB improvement). When using DeEPer, the resonant wavelength shifts in the MRs at different stages are smaller, resulting in a lower crosstalk being accumulated on the desired optical signal, and hence a higher OSNR (see (6)). Considering Figs. 6(a) and 6(b), the average crosstalk power ( $N_p$ ) is reduced by 9.8 dB when using DeEPer. Also, when using DeEPer, the average optical signal power ( $S_p$ ) calculated at different PDs decreases, indicating some power penalty in the system (i.e., 3.9 dB

average power loss when using DeEPer). This power loss is due to a reduction in the dropped power in the MRs when using DeEPer, which can be mitigated through further optimizing the MRs design (e.g., employing a longer (smaller) coupler (gap)). Note that the average power loss without considering PD<sub>4</sub> in Fig. 6 is only 1.5 dB. The results in this section indicate that employing DeEPer considerably improves the OSNR in OINs, and hence their performance and reliability under PV. Also, DeEPer helps reduce the tuning power required for correcting faulty MRs as their resonant wavelengths are closer to the designed resonances when DeEPer is employed (see Fig. 4(b)).

## 5 CONCLUSION

We present DeEPer, an efficient device-level design method that explores the design space of MRs to improve the performance and reliability in optical interconnects. The analytical models as well as the design guidelines required to apply DeEPer to OINs are proposed. DeEPer is experimentally evaluated through fabricating several MRs, in which the resonant wavelength shifts are reduced when using DeEPer. As a system-level case study, we apply DeEPer to a general passive WDM-based OIN, and we indicate that it considerably improves the OSNR in the system (almost 6 dB on average). Results of this work help system designers better understand the impact of MRs design space on realizing high-performance and reliable OINs for MPSoCs.

## ACKNOWLEDGMENT

The authors acknowledge NSERC, and the Silicon Electronic-Photonic Integrated Circuits (Si-EPIC) program for the fabrication and automated measurements.

## REFERENCES

- [1] Y. Arakawa et al. 2013. Silicon Photonics for Next Generation System Integration Platform. *IEEE Communications Magazine* 51, 3 (2013), 72–77.
- [2] M. Bahadori et al. 2016. Crosstalk Penalty in Microring-Based Silicon Photonic Interconnect Systems. *IEEE JLT* 34, 17 (2016), 4043–4052.
- [3] R. G. Beausoleil et al. 2011. Devices and Architectures for Large-Scale Integrated Silicon Photonics Circuits. *Proceeding of SPIE* 7942 (2011), 794204–1–794204–6.
- [4] W. Bogaerts et al. 2012. Silicon Microring Resonators. *Laser and Photonics Reviews* 6, 1 (2012), 47–73.
- [5] S. V. R. Chittamuru et al. 2016. PICO: Mitigating Heterodyne Crosstalk Due to Process Variations and Intermodulation Effects in Photonic NoCs. In *DAC*. 1–6.
- [6] L. Chrostowski et al. 2014. Impact of Fabrication Non-Uniformity on Chip-Scale Silicon Photonic Integrated Circuits. In *OFC*. Th2A.37.
- [7] L. Chrostowski et al. 2015. *Silicon Photonics Design from Devices to Systems*. Cambridge University Press.
- [8] Y. Kokubun et al. 2010. UV Trimming of Polarization-Independent Microring Resonator by Internal Stress and Temperature Control. *Optical Express* 18, 2 (2010), 906–916.
- [9] Z. Li et al. 2012. Reliability Modeling and Management of Nanophotonic On-Chip Networks. *IEEE TVLSI* 20, 1 (2012), 98–111.
- [10] Lumerical Solutions Inc. 2017. Lumerical MODE. (2017). <http://www.lumerical.com/tcad-products/mode/>
- [11] Y. Luo et al. 2016. A Process-Tolerant Ring Modulator Based on Multi-Mode Waveguides. *IEEE Photonics Technology Letters* 28, 13 (2016), 1391–1394.
- [12] M. Mohamed et al. 2014. Reliability-Aware Design Flow for Silicon Photonics On-Chip Interconnect. *IEEE TVLSI* 22, 8 (2014), 1763–1776.
- [13] M. Nikdast et al. 2016. Chip-Scale Silicon Photonic Interconnects: A Formal Study on Fabrication Non-Uniformity. *IEEE JLT* 34, 16 (2016), 3682–3695.
- [14] M. Nikdast et al. 2016. Modeling Fabrication Non-Uniformity in Chip-Scale Silicon Photonic Interconnects. In *DATE*. 115–120.
- [15] X. Wu et al. 2014. SUOR: Sectioned Unidirectional Optical Ring for Chip Multiprocessor. *ACM J. Emerg. Technol. Comput. Syst.* 10, 4 (2014), 29:1–29:25.
- [16] D. X. Xu et al. 2014. Silicon Photonic Integration Platform - Have We Found the Sweet Spot? *IEEE J. Sel. Topics Quantum Electron.* 20, 4 (2014), 189–205.